Philosophical Magazine
First published in 1798

Ensemble averaging stress-strain fields in polycrystalline aggregates with a constrained surface microstructure - Part 2: crystal plasticity

PLEASE SCROLL DOWN FOR ARTICLE

Taylor & Francis
Taylor & Francis Group

Ensemble averaging stress–strain fields in polycrystalline aggregates with a constrained surface microstructure – Part 2: crystal plasticity

A. ZEGHADI†, S. FOREST*†, A.-F. GOURGUES†
and O. BOUAZIZ‡

†Centre des Matériaux/Mines Paris, Paristech, CNRS UMR 7633,
B.P. 87, 91003 Evry Cedex, France
‡ARCELOR Research, Voie Romaine, B.P. 30320,
57283 Maizières-lès-Metz, France

The effect of three-dimensional (3D) grain morphology on the deformation at a free surface in polycrystalline aggregates is investigated by means of a large-scale finite element and statistical approach. For a given two-dimensional surface at $z = 0$ containing 39 grains with given crystal orientations, eight 3D random polycrystalline aggregates are constructed having different 3D grain shapes and orientations except at $z = 0$, based on an original 3D image analysis procedure. They are subjected to overall tensile loading conditions. The continuum crystal plasticity framework is adopted and the resulting plastic strain fields at the free surface $z = 0$ are analyzed. Ensemble average and variance maps of the plastic strain field at the observed free surface are computed. In the case of elastoplastic copper grains, fluctuations ranging between 2% and 80% are found in the equivalent plastic slip level at a given material point of the observed surface from one realization of the microstructure to another. The obtained fields are compared to the prediction based on the associated columnar grain microstructure, often used in the literature.

1. Introduction

Crystal plasticity theory is now a well-established continuum framework aimed at describing the anisotropic plastic behaviour of single and polycrystals, based on the kinematics of plastic slip with respect to active slip systems [1–3]. Finite element simulations relying on crystal plasticity constitutive equations are commonly used to address at least the three following problems:

(1) Texture evolution during deformation processes; plastic deformation in single crystals or grains in polycrystals are associated with lattice rotation which can be estimated by means of the crystal plasticity framework [4–6].

---

*Corresponding author. Email: samuel.forest@ensmp.fr

(2) Comparison between full-field finite element crystal plasticity models of polycrystalline aggregates and simplified homogenization models [7, 8].

(3) Prediction of strain heterogeneities and strain localization phenomena in crystalline solids; deformation incompatibilities from grain to grain due to lattice misorientation result in strongly heterogeneous plastic strain fields in polycrystalline aggregates subjected to various mechanical loading conditions such as tension, shear or rolling [7, 9–11].

Model predictions related to these three issues can be compared to experimental results obtained by quasi-volume measurements like X-ray or neutron diffraction and surface field measurements like grid deformation and Electron Back-Scatter Diffraction (EBSD). The comparison of strain field measurements with finite element predictions requires a detailed description of the grain morphology and initial lattice orientation field on the observed surface. The intrinsically three-dimensional (3D) character of plastic slip processes must be taken into account [12, 13]. This is however not enough to reach quantitative agreement with strain and lattice rotation field measurements [14, 15]. A precise knowledge of the 3D grain morphology below the surface is necessary for a full validation or identification of the continuum model. Considerable effort is required to actually determine the 3D shape of the grains belonging to a given surface. This can be done by successive polishing and EBSD mapping of the polycrystal sample as done with success in [16, 17]. Non-destructive 3D X-ray diffraction analysis represents a promising method to get the actual 3D grain shape and orientation [18, 19]. When this 3D information is not available, one usually considers an ideal columnar morphology deduced from the surface observation by translation with respect to the out-of-plane direction [20], or a more complex random 3D morphology coinciding with the actual one at least at the visible free surfaces [13]. The objective of the present work is to give a quantitative assessment of the bias introduced by such geometrical simplifications on the prediction of the stress–strain fields at the observed free surface. Even though most authors are aware of the major role that the actual 3D grain morphology plays in the development of surface plastic strain field, there seems to be no quantitative estimate of this effect available in the literature.

For that purpose, a large-scale computational and statistical approach is developed aiming at comparing the elastoplastic response of polycrystalline aggregates having different grain shapes and crystal orientations except at a given free surface. A systematic image analysis algorithm for constructing 3D polycrystalline aggregates with a prescribed surface microstructure was described in part 1 of this work [21]. It was used to estimate the 3D surface grain morphology effect in the case of purely elastic grain response. The same reference surface at $z = 0$ as in part 1 is used in part 2 of this work. It is shown in figure 1 and contains 39 grains with fixed orientations. The correspondence between grain number and crystal orientation is given in table 1 of part 1 of this work [21]. Eight out of the 17 polycrystalline aggregates having the surface microstructure of figure 1 in common, as presented in part 1, are considered for the nonlinear simulations of part 2. Fluctuations of the order of $\pm 20\%$ of local stress values at the free surface were found in part 1 for elastic copper grains [21]. The corresponding fluctuation field is given in the present part for elastoplastic copper crystals. In the simulations, grain boundaries are treated as ideal geometric
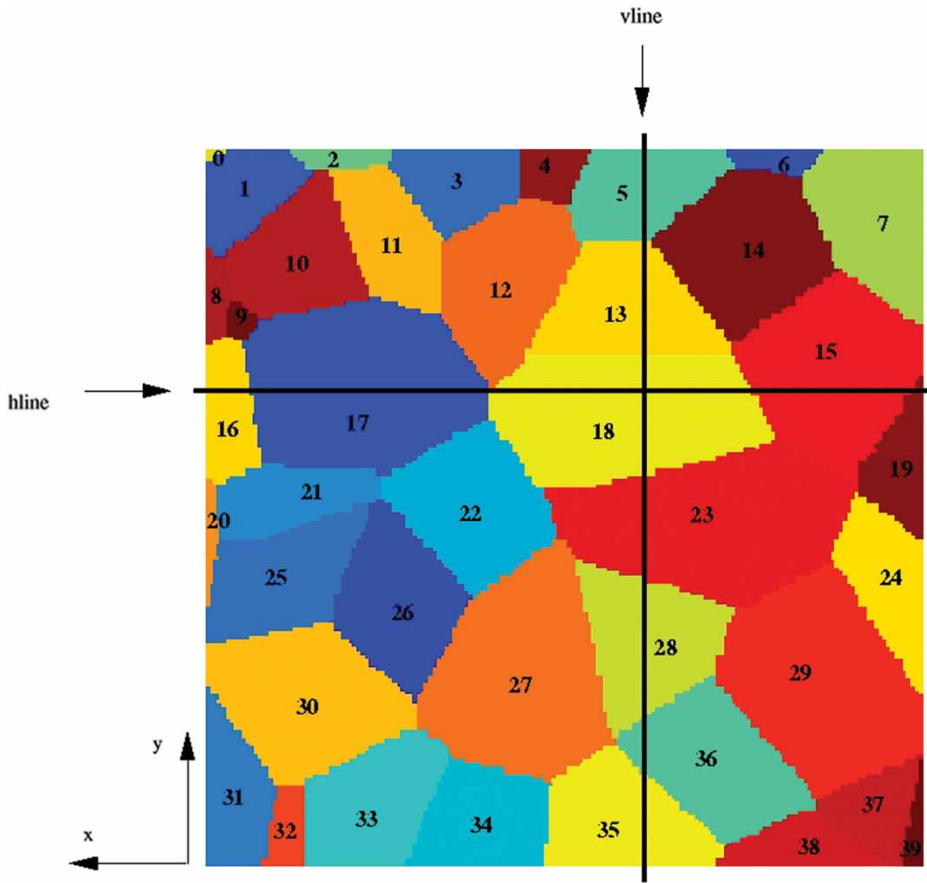
Figure 1.   Reference surface $z = 0$ which is prescribed for the construction of polycrystalline aggregates. All surface grains are labelled from 1 to 39. Two lines *hline* and *vline* have been distinguished along which mechanical variables obtained in the finite element simulations of this work can be plotted.

Table 1.   Values of the material model parameters for single crystal copper (after [33] and [22]).

C_{11} (MPa)			C_{12} (MPa)			C_{44} (MPa)
168 400			121 400			75 390c

r_0 (MPa)	Q (MPa)	b	K (MPa.s$^{1/m}$)	m	h_1	$h_i (i \neq 1)$
40.0	17.0	10.0	2.0	15.0	1.0	1.4

interfaces ensuring continuity of displacement and traction vectors. Diffusion does not play a significant role in the room temperature behaviour of copper polycrystals so that no grain boundary evolution or migration is introduced in the model which concentrates on the plastic quasi-rate-independent deformation of grains.

Standard crystal plasticity constitutive equations are recalled in section 2. Section 3 deals with the influence of sample thickness, i.e. the number of grains within the thickness of the parallelepipedic polycrystalline specimens, on the plastic strain field observed at the constrained free surface. Strain heterogeneities computed at the constrained free surface for the eight analyzed specimens subjected to simple tension are described in section 4. The proposed statistical approach consists in ensemble averaging the plastic strain field at the constrained free surface and in computing the corresponding variance field (section 5).

The notations used throughout this work have been settled in part 1 [21]. Regarding statistical operations used throughout this work, we simply recall here the notions of volume average and ensemble average for a field quantity f taking the value $f(\mathbf{x})$ at position $\mathbf{x}$ of a material point in a given realization of the volume element V of the microstructure. The volume (spatial) average of f over a given volume V is denoted by

$$\langle f \rangle := \frac{1}{V} \int_V f(\mathbf{x}) \, dV \tag{1}$$

Specific notations are introduced for the volume averaged stress and strain components

$$\Sigma_{22} := \langle \sigma_{22} \rangle, \quad E_{22} := \langle \varepsilon_{22} \rangle \tag{2}$$

The ensemble average of the values $f^i(\mathbf{x})$ of the quantity f taken at $\mathbf{x}$ in N realizations of the microstructure in a volume V is

$$\bar{f}(\mathbf{x}) := \frac{1}{N} \sum_{i=1}^{N} f^i(\mathbf{x}) \tag{3}$$

The corresponding variance D and relative variance ϵ operators are defined for a field $f(\mathbf{x})$ by

$$D(f(\mathbf{x})) := \sqrt{\frac{1}{N} \sum_{i=1}^{N} (f^i(\mathbf{x}) - \bar{f}(\mathbf{x}))^2}, \quad \epsilon(f(\mathbf{x})) = \frac{D(f(\mathbf{x}))}{\bar{f}(\mathbf{x})} \tag{4}$$

2. Constitutive equations and material parameters

The formulation of the crystal plasticity model adopted in this work has been originally formulated in [22] within the small strain framework. The classical decomposition of strain rate into elastic and plastic parts reads:

$$\dot{\varepsilon} = \dot{\varepsilon}^e + \dot{\varepsilon}^p \tag{5}$$

Plastic strain rate is the sum of elementary slip contributions with respect to n crystal slip systems. The crystallographic nature of plastic slip is taken into account by means of the orientation tensor P^s. Slip systems are geometrically defined by

vectors $\mathbf{n}^s$ and $\mathbf{l}^s$ which are respectively the normal to the slip plane and the slip direction:

$$\dot{\varepsilon}^p = \sum_{s=1}^{n} \dot{\gamma}^s \, \mathsf{P}^s, \quad \mathsf{P}^s = \frac{1}{2}(\mathbf{l}^s \otimes \mathbf{n}^s + \mathbf{n}^s \otimes \mathbf{l}^s) \tag{6}$$

Crystal plasticity is assumed to be driven by the resolved shear stress on slip system s:

$$\tau^s = \sigma : \mathsf{P}^s \tag{7}$$

A phenomenological viscoplastic flow rule based on the Schmid law is adopted to compute the individual slip rates depending on τ^s and on hardening variables:

$$\dot{\gamma}^s = \dot{v}^s \mathrm{sign}(\tau^s) \tag{8}$$

$$\dot{v}^s = \left\langle \frac{|\tau^s| - r^s}{K} \right\rangle^m \quad \text{with} \quad \langle x \rangle = \mathrm{Max}(x, 0) \quad \text{and} \quad v^s(t=0) = 0 \tag{9}$$

where r^s is the isotropic hardening variable attached to slip system s. An explicit nonlinear hardening rule is chosen:

$$r^s = r_0 + Q \sum_r h_{sr}\left(1 - e^{-bv^r}\right) \tag{10}$$

Self- and cross-hardening between slip systems is accounted for via the interaction matrix h_{sr}.

The parameters of this constitutive model were calibrated from results for single and bi-crystals in the case of copper in [22]. They are adopted for the present simulations and given in table 1. The viscosity parameters K, m account for the slight rate-dependence of copper at room temperature. Note that the kinematic hardening term introduced in [22] and identified from cyclic tests is not used in the present work for simplicity. The twelve octahedral slip systems of cubic face centered crystals are considered. The slip directions $\mathbf{l}^s$ are the six directions $\langle 011 \rangle$ and the slip planes with normal $\mathbf{n}^s$ are the four planes $\{111\}$.

In the present work, we also want to compare lattice rotation maps obtained for several realizations, because, in practice, computed lattice rotation fields can be compared to experimental EBSD maps. It is then necessary to include explicitly lattice orientation evolution into the model. In the following, the finite-deformation crystal plasticity framework is briefly recalled. A detailed description of the large-deformation theory of single crystals model can be found for instance in [1–3, 10]. Based on the introduction of an intermediate stress-released configuration, a multiplicative decomposition of the deformation gradient is postulated as:

$$\mathsf{F} = \mathsf{E} \cdot \mathsf{P}, \quad \text{with} \quad \mathsf{E} = \mathsf{S}^e \cdot \mathsf{R}^e \tag{11}$$

In the intermediate isoclinic configuration, the crystal orientation with respect to the laboratory axes is the same as in the initial one. The polar decomposition of the elastic part of deformation involves the rotation part R^e and the symmetric elastic stretch part S^e. In metals the elastic stretch remains small so that the rotation

R^e can be interpreted as the crystal lattice rotation. The kinematics of plastic slip is given by

$$\dot{\mathsf{P}} \cdot \mathsf{P}^{-1} = \sum_{s=1}^{n} \dot{\gamma}^s \, \mathbf{l}^s \otimes \mathbf{n}^s \qquad (12)$$

In the case of limited strains and rotations, it is sufficient to consider a small-strain and small-rotation framework deduced from the full finite deformation model, as done in [13]. The advantage of this formulation is mainly the numerical efficiency because it reduces the geometrical nonlinearity of the problem. In the case of small strain and small rotations, the previous decomposition is written:

$$\mathsf{F} = \mathsf{S}^e \cdot \mathsf{R}^e \cdot \mathsf{P} \simeq (1 + \varepsilon^e) \cdot (1 + \omega^e) \cdot (1 + \varepsilon^p + \omega^p) \simeq 1 + \varepsilon^e + \omega^e + \varepsilon^p + \omega^p \quad (13)$$

Small elastic strains and rotations are respectively ε^e and ω^e. They are respectively symmetric and skew-symmetric second rank tensors. Their plastic counterparts are the tensors ε^p and ω^p. The velocity gradient becomes:

$$\dot{\mathsf{F}} \cdot \mathsf{F}^{-1} \simeq \dot{\varepsilon}^e + \dot{\omega}^e + \dot{\varepsilon}^p + \dot{\omega}^p = \dot{\varepsilon} + \dot{\omega}, \quad \text{with} \quad \dot{\varepsilon} = \dot{\varepsilon}^e + \dot{\varepsilon}^p, \quad \dot{\omega} = \dot{\omega}^e + \dot{\omega}^p \quad (14)$$

As a result of equation (12), the plastic deformation and rotation rates become:

$$\dot{\varepsilon}^p = \frac{1}{2} \sum_{s=1}^{n} \dot{\gamma}^s \, (\mathbf{l}^s \otimes \mathbf{n}^s + \mathbf{n}^s \otimes \mathbf{l}^s), \quad \dot{\omega}^p = \frac{1}{2} \sum_{s=1}^{n} \dot{\gamma}^s \, (\mathbf{l}^s \otimes \mathbf{n}^s - \mathbf{n}^s \otimes \mathbf{l}^s) \qquad (15)$$

In the context of small deformations, lattice rotation is accounted for by tensor ω^e. The normal to the slip plane $\mathbf{n}^s$ and the slip direction $\mathbf{l}^s$ are updated as follows:

$$\mathbf{n}^s = \omega^e \cdot \mathbf{n}_0^s, \quad \mathbf{l}^s = \omega^e \cdot \mathbf{l}_0^s \qquad (16)$$

In the presentation of the results of the finite element simulations performed within this crystal plasticity framework, the following measure γ_{eq} of cumulative plastic slip will be used extensively

$$\gamma_{\mathrm{eq}} = \sum_{i=1}^{n} v^s \qquad (17)$$

The model is implemented in the finite element package Zset [23]. Implicit global resolution and local integration schemes are used, based on Newton formulations of the algorithms.

3. Spatial range of the plastic strain field

The question of the optimal thickness of the polycrystalline samples considered to study the stress–strain fields at a given free surface was treated in the case of aniso-tropic linear elastic behaviour of the grains in part 1 of this work [21]. A thickness of two grains on average was adopted. This question has to be reconsidered in the elastoplastic case. For that purpose, three finite element simulations of the tensile

response in direction y of three samples with common grain morphologies and crystal orientations but different thicknesses were performed. The grain morphology at $z = 0$ is given in figure 1. The three samples are slices with different thicknesses of a large given 3D polycrystalline aggregate, containing the constrained free surface. The results are shown in figure 2 in the form of plastic slip maps at the free surface of the three samples. The sample thickness respectively is 1, 1.5 and 2 grains on average. There are significant differences in the local values of the amount of equivalent slip at the free surface between the pictures 2a and b respectively obtained for thicknesses of 1 and 1.5 grains. For example, grains 35, 34, 30, and 27 remain almost plastically undeformed if a one-grain thick sample is considered, whereas plastic slip is stronger in these grains in the 1.5-grain thick sample. On the other hand, there is a large zone of plastic deformation at the junction of grains 15, 18, 19 and 23 in map 2a. The plastic deformation is limited to the 23/29 grain boundary region for the thicker sample 2b. In contrast, pictures 2b and c are very similar. The plastic zones are similar, except at the junction of the grains 36, 38, 37 and 29. These similarities seem to indicate a convergence of the plastic strain field at the constrained free surface, even though computations with even thicker samples would be necessary to give a definitive statement on this convergence. In fact, the local values of plastic strain do not vary by more than 15% from map 2b to map 2c.

The analysis of the average surface effect in [7, 24] for f.c.c polycrystals also leads to the prediction of a rather short-range action of plastic deformation. The latter references analyze the average fields and their variance in random polycrystals as a function of the distance to a free surface or to a grain boundary. The range of average stress perturbed by the presence of a free surface or a grain boundary is found to be less than the size of one grain. However, in this analysis, the free surface morphology was not kept constant so that obtained information is of a different nature from the results presented in this section.

Previous calculations bring some elements to the solution of the longstanding question of the range of stress–strain fields in crystal plasticity. What is the acting range or influence range of grains within a polycrystal during deformation? In particular, how many layers of grains influence the local elastoplastic response of the polycrystal at a free surface?

From the three computations presented in this section, we can estimate the range of plastic action to be larger than or of the order of two grain sizes. So, at least two grain layers are needed to determine the main features of the plastic strain field at the free surface. This means that the use of thicker samples would not significantly modify the response of the observed free surface. As a compromise between the convergence of local fields at the free surface and computation cost associated with large number of grains, a sample thickness of two grain sizes on average has been retained in the following computations.

The mesh size used for the computations of elastoplastic crystals is larger than that used in the first part of this work dedicated to linear behaviour, with a view to obtaining reasonable computation times. A mesh density of 1434 degrees of freedom (d.o.f.) per grain was retained as a result of the mesh sensitivity studies presented in [7, 25]. This density still allows a detailed description of intragranular mechanical fields. The retained values for mesh density and sample thickness lead to parallelepipedic meshes made of $30 \times 30 \times 10$ quadratic elements, corresponding
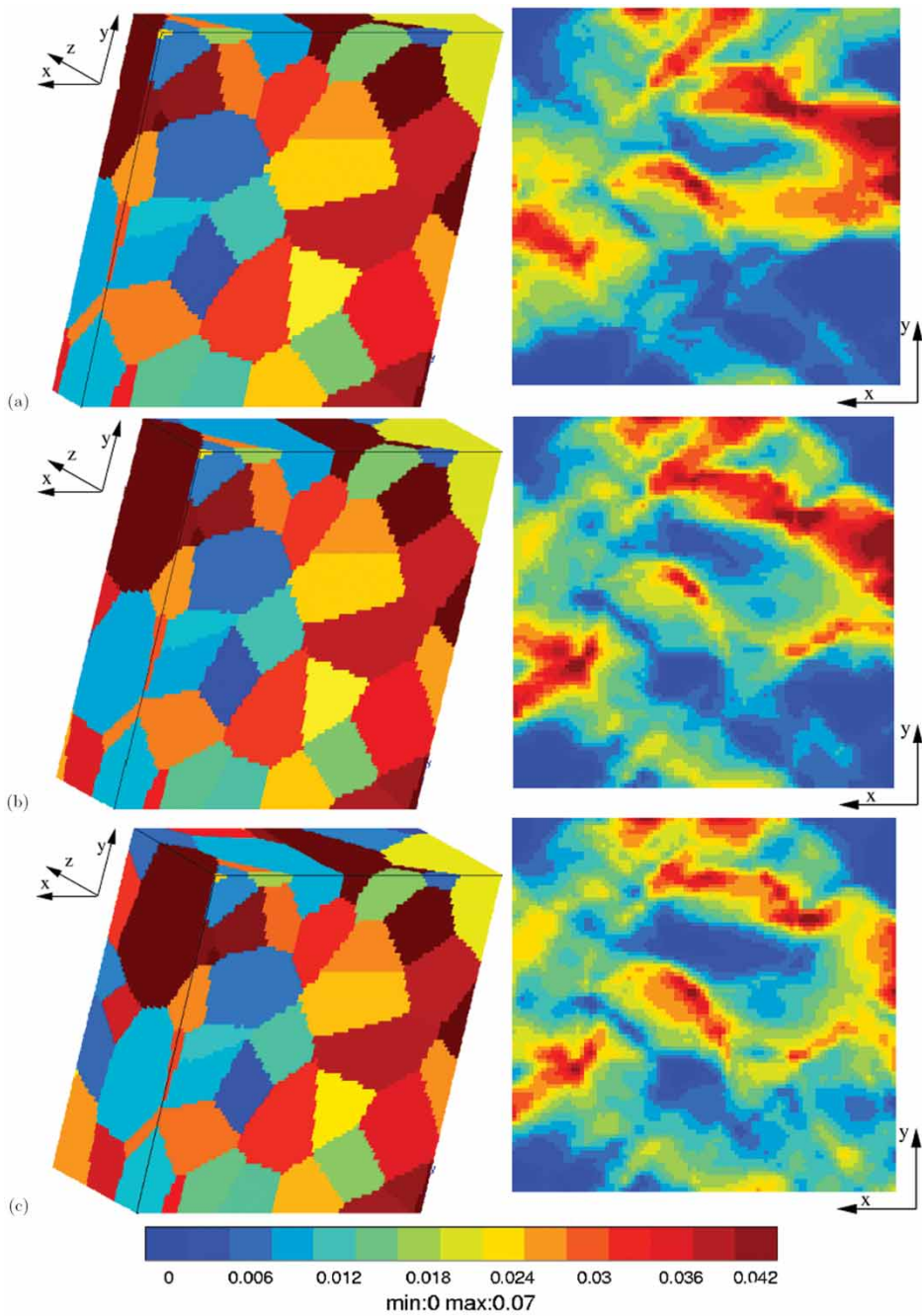
Figure 2. Influence of the sample thickness on the plastic strain field at the free surface. Three different average numbers of grains within the thickness are considered: (a) 1 grain, (b) 1.5 grain, (c) 2 grains. The cumulative plastic slip γ_{eq} fields are given for $E_{22} = 0.01$. The three samples are slices with different thicknesses of a large given 3D polycrystalline aggregate containing the constrained free surface of figure 1.

to 121 923 d.o.f. The average number of grains in each specimen is 85 with a variance of nine grains.

4. Plastic strain heterogeneities at the constrained free surface

Nine polycrystalline aggregates sharing the free surface grain morphology of figure 1 at $z = 0$ were subjected to simple tension in the direction y up to 2% overall strain $E_{22} = \langle \varepsilon_{22} \rangle$. The eight samples are random polycrystals with a constrained free surface and with a microstructure obtained by means of the grain generation algorithm presented in part 1 of this work (section 2 of part 1). The ninth sample is a columnar microstructure obtained by extension in the z-direction of the grain picture of figure 1. A representation of this columnar microstructure is provided in figure 5 of part 1 [21]. It is recalled that for each sample the two-dimensional (2D) surface grain morphology and initial lattice orientation of all the 39 surface grains are identical. The boundary conditions for applying a mean axial deformation E_{22} to a sample V are the mixed homogeneous conditions used in part 1 of this work [21]. The displacement U_2 is fixed to zero at $y = 0$ and to a prescribed value at the upper part. All lateral surfaces, including the constrained surface $z = 0$, are free of forces. A schematic description of these boundary conditions is given in figure 9 of part 1 [21]. A parallel computing method based on subdomain decomposition and described in section 3 of part 1, was used for each finite element computation. The simulation of each tensile test distributed among four processors required two months computation time.

The overall tensile curves of the nine specimens are provided in figure 3 where the volume average stress Σ_{22} is plotted as a function of the volume average strain E_{22}. The overall stress level does not vary by more than 2% from one realization of the microstructure to another. This shows that the variation of grain morphology and
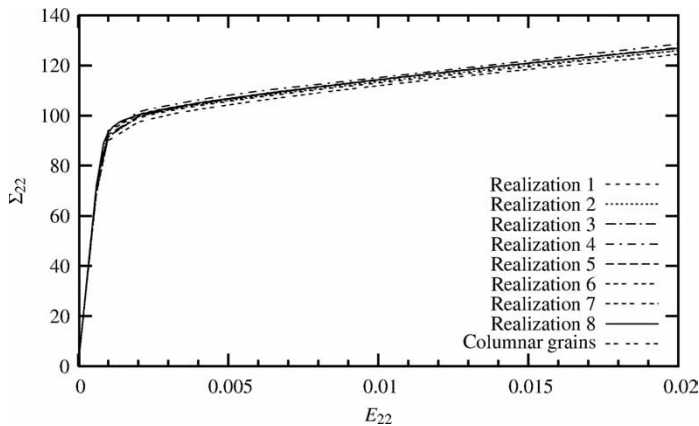

Figure 3. Overall tensile curves of the nine polycrystalline aggregates with constrained free surface geometry. For each sample, the mean stress component $\Sigma_{22} = \langle \sigma_{22} \rangle$ is given as a function of the mean strain component $E_{22} = \langle \varepsilon_{22} \rangle$.

grain environment beneath the free surface does not affect the overall response of the material significantly.

In contrast to the overall behaviour, the local material response is strongly affected by the change of grain morphology and granular environment below the free surface. The maps of the cumulative plastic slip γ_{eq} at the free surface $z = 0$ are given in figure 4 for five different realizations. The values are normalized by the corresponding ensemble average value over all volumes. The distribution of the cumulative plastic slip turns out to be strongly heterogeneous. The maps show the development of bands of intense plastic deformation generally oriented at about $45°$ from the tensile direction, in which the plastic strain can reach up to five times the prescribed mean deformation. These bands, in red in the maps of figure 4, usually extend over several grains thus crossing grain boundaries. This is in contrast to the stress–strain maps obtained in the case of purely elastic response of polycrystalline aggregates investigated in section 5 of part 1 [21]. The plastic strain maps of figure 4 can be compared directly to the stress (or equivalently) strain maps of figure 10 in part 1, since the surface grain morphology and lattice orientations are the same. In anisotropic elastic crystals, stress–strain concentrations systematically take place close to grain boundaries and junctions. It is not the case in elastoplastic crystals for which deformation bands extend over several grains crossing grain boundaries and grain cores. That is why the grain boundaries have been drawn in bold in the maps of figure 4 in order to identify the individual grain shapes. The number and location of plastic strain bands differ from one realization to another. Confined plastic strain zones inside the grains and plastic strain concentrations along some grain boundaries are also observed.

The existence of bands or zones of plastic deformation extending over two or three grains, or even more, was already observed in the simulation of the response of f.c.c. polycrystals in [7] for instance. There is also clear experimental evidence of this plastic phenomenon through strain field measurements [26]. These authors report the development of networks of bands of intense deformation with a spacing and a range equivalent to about 10 grains. Unfortunately, the size of the simulated surface is too small here to really obtain reliable information about the length and spacing of such bands so that no quantitative comparison is possible yet with this kind of experimental results.

The local values of cumulative plastic slip in a given surface grain can vary by a factor of more than 6 from one realization to another. Grain 15, for example, displays different cumulative plastic slip levels: Only 5% of the surface of this grain exhibits relative plastic slip values larger than 1.5 in figure 4a whereas 80% of the grain reaches this value in figure 4b. In figure 4d, 5% of the surface of grain 23 has a relative plastic slip level larger than 1.8 whereas it represents 15% of the same grain in figure 4a, 40% in figure 4b and 50% in figure 4c. Slip in grain 21 is quasi-homogeneous in figure 4d, with a relative plastic slip level larger than 2. This quasi-homogeneous plastic slip distribution is found in the same grain in figure 4c but for a level equal to 0.4. Grain 30 is almost plastically undeformed in realizations 4a and d. The core of the same grain displays relative plastic slip levels higher than 1.4 in realization 4b. These large differences in the level of the cumulative plastic slip from one realization to another are observed in large grains as well as in smaller ones.
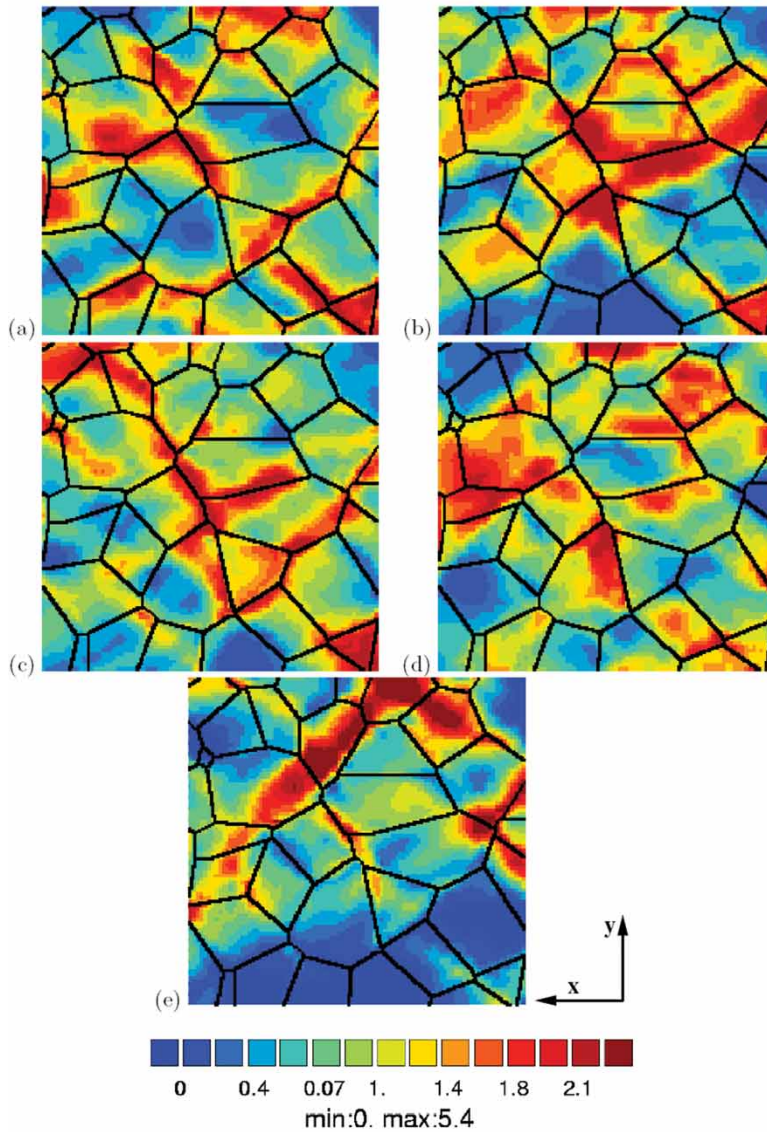
Figure 4. Cumulative plastic slip distribution $\gamma_{eq}(\mathbf{x})$ normalized by the global mean cumulative plastic slip $\overline{\langle \gamma_{eq} \rangle}$ for four different 3D realizations (a)–(d) of the polycrystalline aggregates with a constrained surface geometry. The tensile loading direction y is vertical. The plane of observation is the constrained free surface $z = 0$, the geometry of which was given in figure 1. The plastic slip map is also given for the columnar grain microstructure in (e). Grain boundaries are in bold. The prescribed overall tensile strain is $E_{22} = 0.02$. The value of $\overline{\langle \gamma_{eq} \rangle}$ was 0.0442.
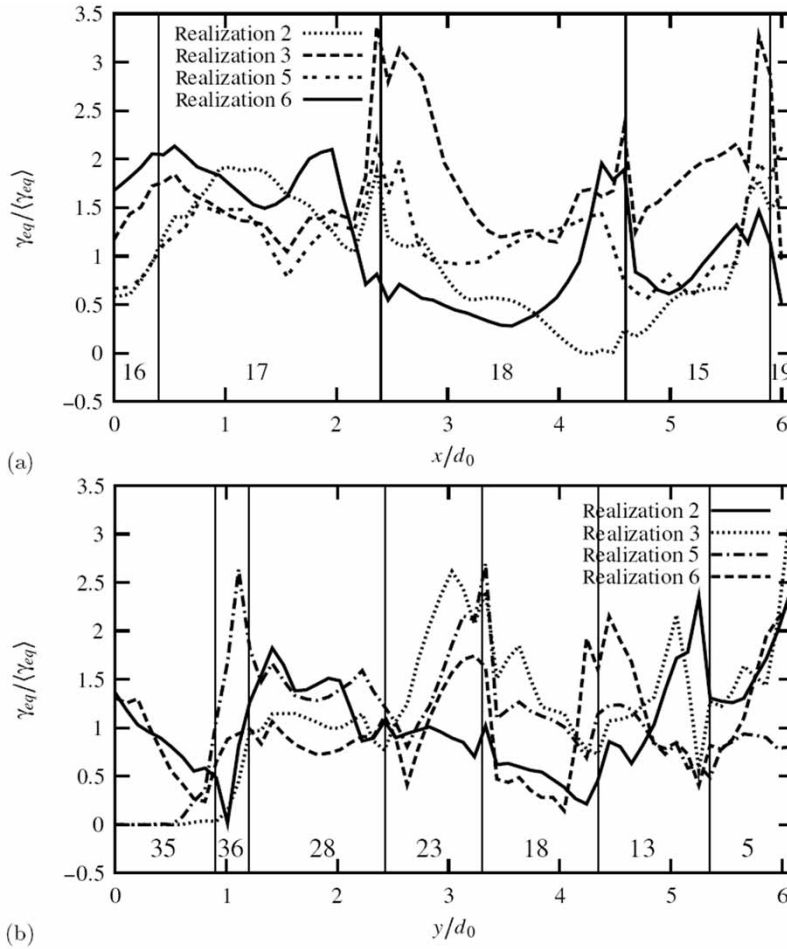
Figure 5. Cumulative plastic slip profiles along the lines *hline* (a) and *vline* (b) of figure 1 for four different realizations of polycrystalline aggregates with a prescribed free surface and subjected to simple tension. The stress distribution is normalized by the global mean stress $\overline{\langle\gamma_{eq}\rangle}$ over all realizations. The vertical lines indicate the *x*-position of the intersection between the grain boundaries and the line *hline*. The labels of the corresponding grains are recalled. The prescribed overall tensile strain is $E_{22} = 0.02$.

This huge scatter in the plastic slip values is shown in a more quantitative way in the curves of figure 5. The relative cumulative plastic slip level is plotted along the horizontal line *hline* and along vertical line *vline* drawn on the constrained free surface of figure 1. Line *hline* crosses five large grains whereas line *vline* crosses seven smaller grains. Large differences arise at three different levels:

- *From grain to grain* for a given realization of the microstructure: The ensemble average plastic slip can vary by a factor of 5.
- *Inside a grain* for a given realization: Steep plastic strain gradients are observed for instance in grains 15 and 13.

- *From one realization to another*: The mean relative plastic slip in grain 18 is 3 times higher for the realization 3 than in the realization 6. Plastic slip is homogeneous in grain 35 in realizations 3 and 5. The same grain displays a steep plastic strain gradient in realizations 2 and 6.

Figure 4e gives the field of relative cumulative plastic slip in the extreme case of a columnar grain morphology. In the literature, such a morphology is very often used to compare the results of strain field measurements and of finite element computations [11, 12, 15]. The deformation field found in the columnar grains is characterized by the formation of well-defined deformation bands, one of them crossing five grains of the surface. The lower part of the surface contains plastically quasi-undeformed grains. As a matter of fact, the found strain field significantly differs from the results found for all random microstructures considered previously. This proves that strain fields measured at the free surface of polycrystals may strongly deviate from finite element predictions based on the hypothesis of columnar morphology, except when the columnar morphology is close to the actual one, like in metal thin films or coatings having a so-called 'bamboo' microstructure.

It is not possible to find out the precise reason why a certain underlying grain morphology will produce high plastic deformation in a given grain and why a different morphology will not, because this is the result of complex interaction between grain geometry and combinations of lattice orientations. However, figure 6 illustrates the influence of grain shape and size on the heterogeneity of strain in two specific cases. Figure 6a shows the section of two realizations of the microstructure along a plane crossing the grains 25, 26, 27, 28, 29, 24. It is possible to visualize, at least partly, the shape of the grains crossed by this line in both realizations. In particular, orange grain 27 is small in the left realization and significantly larger in the right picture. This has a strong influence on the stress concentration field of figure 6b, on the one hand, and on the field of relative plastic slip in figure 6c, on the other hand. Figure 6b obtained for an anisotropic elastic behaviour is taken from the results of part 1 of this work [21]. The pictures of figure 6c are reproduced from the maps of figure 4. In figure 6b, grain 27 exhibits high stresses in the left realization and low stresses in the right realization. In figure 6c, the same grain is almost plastically undeformed on the left and displays high plastic slip levels on the right. This shows that a drastic change in shape of a grain can result in a dramatic change in local mechanical response, even though its crystal orientation and that of its neighbours cut by the constrained surface are the same. This holds true for both elastic and plastic behaviour.

5. Ensemble average and variance of the fields

The previous field of plastic slip at the constrained free surface can be ensemble averaged, meaning that a value of cumulative plastic slip is attributed to each pixel of figure 1, equal to the mean value of γ_{eq} from the eight simulated realizations. Such a procedure has already been applied to the stress field and discussed in part 1 of this work [21].
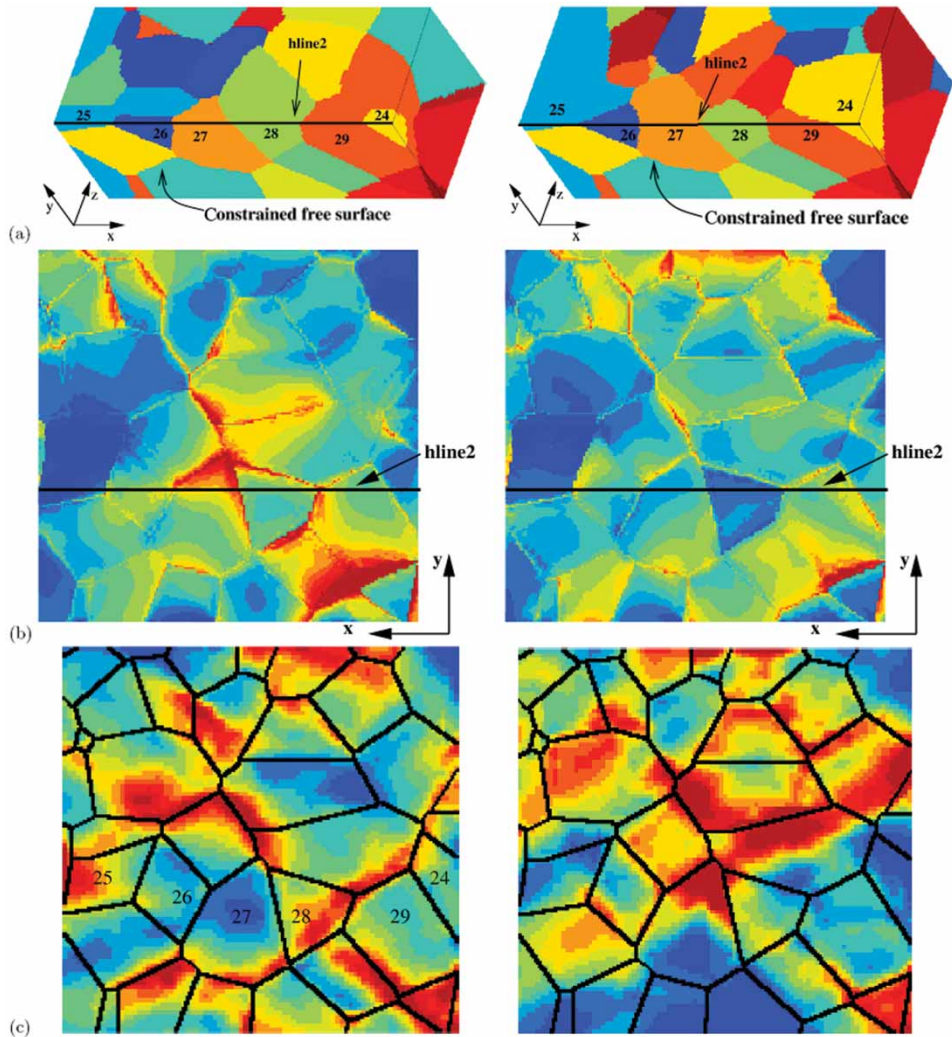
Figure 6. Influence of the 3D grain shape on the stress–strain levels at the constrained free surface. Two realizations of the polycrystalline aggregates with a constrained free surface geometry have been cut along a plane perpendicular to the free surface and containing horizontal line *hline*2, see (a). The von Mises equivalent stress fields obtained under the assumption of an elastic local response, are shown in (b). The corresponding results for an elastoplastic local response are shown in (c), the cumulative plastic slip maps (the colour scale is the same as in figure 4).

5.1. *Plastic slip field*

The map of the ensemble averaged cumulative plastic slip $\overline{\gamma_{eq}}(\mathbf{x})$ is given in figure 7a. As a result of the averaging procedure, the obtained field is significantly smoother than the fields corresponding to the individual realizations shown in figure 4. The amount of plastic slip is normalized by the ensemble and volume averaged plastic slip
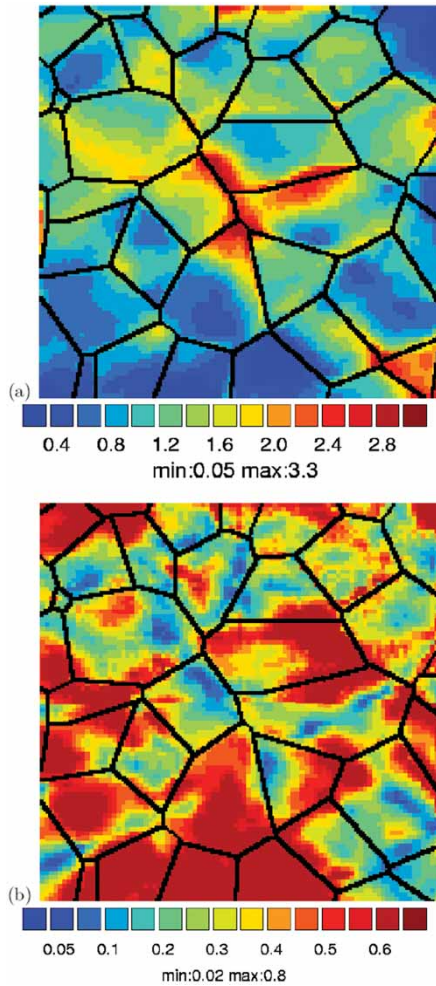
Figure 7.   (a) Ensemble average of the cumulative plastic slip field $\overline{\gamma}_{eq}(\mathbf{x})/\langle\gamma_{eq}\rangle$ at the constrained free surface of the polycrystalline aggregates in tension. (b) Relative variance $D(\gamma_{eq})(\mathbf{x})/\overline{\gamma}_{eq}(\mathbf{x})$ of the local plastic slip at the constrained free surface. Tension is applied along vertical direction y. The prescribed overall tensile strain is $E_{22} = 0.02$.

$\overline{\langle\gamma_{eq}\rangle}$, giving a plastic slip concentration factor. The ensemble averaged relative plastic slip ranges from 0.05 to 3.3, which shows that, locally, the plastic slip concentration factor can be higher than 3. The map also shows that grains 30, 31, 32, 33, 34, 35 remain, on average, plastically undeformed. In contrast, the map of the ensemble averaged plastic strain reveals that there is a high probability of triggering high plastic strain values, namely, in the centre of the free surface at the junction between grains 18, 22, 23, 27 and 28. In spite of the strongly different plastic strain distributions observed in the different realizations of the microstructures, the ensemble averaging procedure reveals the existence of a weak zone in the samples. A useful

application of such an ensemble average map of plastic slip would be to determine, before experimental testing, the zone of the surface where a grid for strain field measurement should be located in order to capture sufficiently high strain or strain gradient levels.

The map of ensemble average plastic slip can be compared to the map of ensemble average stresses established for the same microstructure in the case of a purely elastic response of the grains and shown in figure 13a of part 1 of this work [21]. The field of ensemble averaged stress concentration factors for elastic grains is less heterogeneous than the corresponding map of plastic strain localization factors. The zone of high stress concentration at the boundaries of grains 18, 22, 23, 27, 28 coincides with the zone of high plastic slip predicted by the elastoplastic analysis.

The map of ensemble averaged plastic slip can also be compared to the particular plastic slip map found in the case of a columnar microstructure shown in figure 4e. These maps are found to differ significantly, in contrast to the similarities observed in the case of a purely elastic behaviour as noticed in section 5.2 of part 1 [21]. In particular, the computation based on the columnar morphology fails to reveal the central zone of the surface as the location of most probable slip activity. The choice of the columnar morphology definitely introduces a bias in the estimation of the surface plastic strain field.

The fluctuations of plastic slip observed in the different realizations are characterized by the field of the relative variance $\epsilon(\gamma_{eq}(\mathbf{x})) = D(\gamma_{eq}(\mathbf{x}))/\overline{\gamma_{eq}}(\mathbf{x})$ shown in figure 7b. Note that the local variance at a point $\mathbf{x}$ is normalized by the mean value at the same point $\mathbf{x}$ (see equation (4)). Local plastic slip displays huge fluctuations from one realization to another that range between 2% and 80%. In 15 out of the 39 surface grains, the relative variance is larger than 60%. Note the entirely red grains 32, 33, 34, 35, close to the bottom boundary and the grains 18, 21, 23 and 27 in the centre of the image. Interestingly, the zones of high fluctuations are neither limited to grain boundaries nor to the outer boundary of the surface where boundary conditions are applied. Instead, large regions of grains are characterized by large fluctuations of plastic slip from one realization to another. The variance map shows in a striking way that changing the morphology of grains below the surface results in tremendous changes in the distribution of plastic deformation at the surface.

The ensemble averaged value and variance of the relative equivalent plastic slip is given along the horizontal line *hline* in figure 8. The ensemble average relative plastic slip curve is rather smooth and oscillates between 0.6 and 2 in the grains crossed by the line *hline* of figure 1. The scatter around this mean value is very high reaching $\pm 50\%$, especially in the grains 18 and 15, as shown by the intervals of confidence $\pm D(\gamma_{eq}(\mathbf{x}))/\overline{\gamma_{eq}}(\mathbf{x})$.

The local variance also gives information about the precision of the estimation of the local mean, by dividing the variance by $\sqrt{8}$, 8 being the number of realizations. Due to the low number of realizations considered in the plastic case, the precision in the estimation of the local mean plastic slip is rather poor: from 0.6% to 28% error from point to point. A better precision can only be obtained by increasing the number of realizations. However, picture 7a is not expected to change drastically by adding more realizations, especially, the location of the zones of intense plastic slip activity being already well defined. Another consequence of the low number
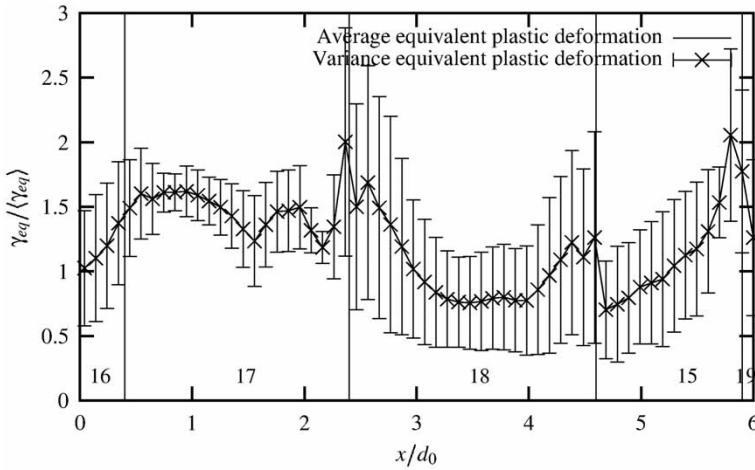
Figure 8. Ensemble average and variance of the cumulative plastic slip profile along the line *hline* belonging to the constrained free surface of figure 1. The local value $\gamma_{eq}(\mathbf{x})$ is normalized by the mean value of the ensemble average of plastic slip $\overline{\langle \gamma_{eq} \rangle}$. The vertical lines indicate the intersection of grain boundaries with line *hline*. The prescribed overall tensile strain is $E_{22} = 0.02$.

of considered realizations is the fact that the values of relative variance given in figure 7b may well be underestimated.

5.2. *Lattice rotation field*

In the previous sections, attention was focused on the evaluation of the plastic strain field. Another important variable in crystal plasticity is the amount of lattice rotation undergone by each material point. The constitutive crystal plasticity framework described in section 2 provides an evaluation of the lattice rotation tensor at each integration point of the finite element analysis. Such predicted lattice rotation maps are given in figure 9. The strong interest of such maps is that they can be compared directly to experimental results of EBSD analyses [27]. At each material point, lattice rotation with respect to the initial lattice orientation at that point is characterized by a rotation axis and a minimal rotation angle $\phi_c(\mathbf{x})$. The absolute value $|\phi_c|$ is mapped for four realizations in figure 9. The contours show that lattice rotation take values ranging between $0.02°$ and $4°$ at the considered mean strain level $E_{22} = 0.02$. Again, bold lines corresponding to the grain boundaries are superimposed on the contour maps.

The heterogeneity of lattice rotation is strong from grain to grain, and inside the grains, in all simulated microstructures. In the realization shown in figure 9a for instance, lattice rotations larger than $2°$ take place in most parts of grains 7, 12, 14, 15 and 19 whereas the crystal orientation is practically unchanged in grains 10, 30 and 33. Strong lattice rotation gradients, also called lattice curvature, are observed in grains 15, 17 and 26 in realization 9b. Lattice curvature is generally observed close to grain boundaries, as in grains 30, 29, 24 and 5 in realization 9c. The development of
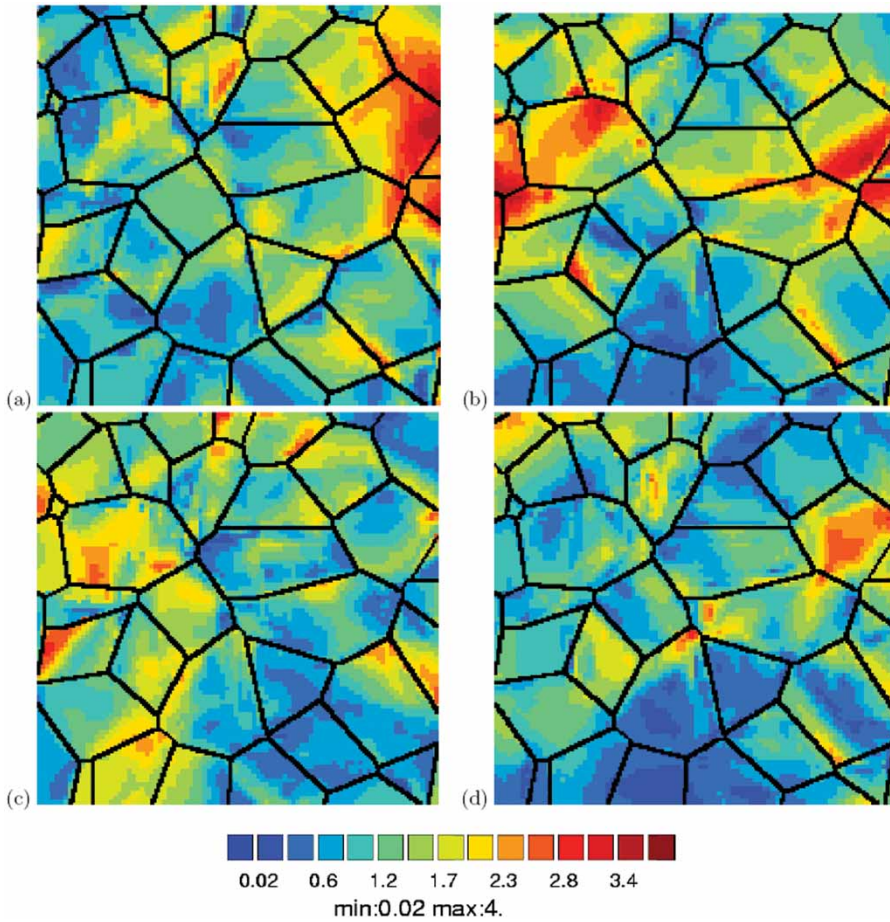
Figure 9.   Lattice rotation maps (in degrees) for four different polycrystalline aggregates with a prescribed free surface geometry. The mapped quantity is the positive part of the lattice rotation angle $\phi_c(\mathbf{x})$. The overall tensile strain is $E_{22} = 0.02$. The tensile direction y is vertical. The four realizations (a)–(d) are the same as those presented in figure 4.

lattice rotation within a given grain strongly depends on the grain morphology below the free surface. In grain 17, for instance, lattice rotations larger than $2.3°$ are observed for realization 9b. They remain smaller than $1.7°$ in the same grain for the realization 9d. This statement holds true for grain 33 in realizations 9a and 9b.

The ensemble averaged lattice rotation field $\overline{|\phi_c|}(\mathbf{x})$ at $E_{22} = 0.02$ is computed from the eight realizations of the field. It is shown in figure 10a. The mean rotation field is found to be rather homogeneous inside the grains but strongly heterogeneous from grain to grain. Lattice orientation is almost unchanged in most of the bottom grains whereas significant lattice rotation takes place in the mid and upper part of the surface. The fluctuations of lattice rotation from one realization to another are generally very high close to grain boundaries. This is the case for instance in grains
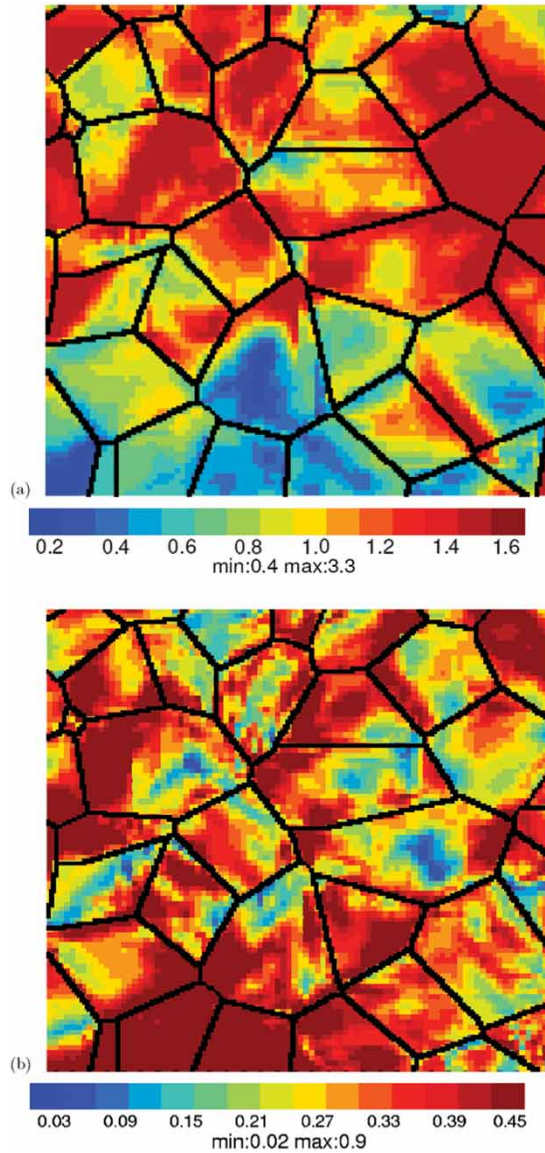
Figure 10.   (a) Ensemble average of the lattice rotation angle field $\overline{\phi_c}(\mathbf{x})$ (in degree) at the constrained free surface of the polycrystalline aggregates in tension. (b) Field of the relative variance $D(\phi_c)(\mathbf{x})/\overline{\phi_c}(\mathbf{x})$ of the local lattice rotation at the constrained free surface. Tension is applied in the vertical direction y. The prescribed overall tensile strain is $E_{22} = 0.02$.

5, 12, 14, 17, 18, 25, 30 according to the variance map of figure 10b. Large fluctuations of lattice rotation are observed in the bottom grains where stringent displacement-based boundary conditions are applied. But the fluctuations are also significant in the central zone of the surface made of the cluster of grains 18, 22, 23, 27, 28.

A striking feature of the variance map is that in 16 out of 39 grains, the relative scatter is larger than 45%. It shows that the development of lattice rotations at the surface strongly depends on the underlying grain morphology. This should be taken into account when comparing the result of EBSD field measurements and the corresponding finite element simulations within the crystal plasticity framework.

6. Conclusions

A large-scale computational and statistical approach has been presented that gives accurate quantitative estimations of the variance of plastic activity at the surface of a polycrystalline aggregate when the morphology of grains below the surface is changed. Strong fluctuations were expected but accurate numbers are provided in this work for the first time. The main results are:

- The plastic deformation band structure that develops at the free surface of polycrystalline sample subjected to uniaxial overall tension strongly depends on the 3D morphology of the grains below the free surface, over a thickness of at least twice the average grain size.
- Ensemble average fields of plastic slip activity and of lattice rotation were provided based on the results of the tensile deformation of eight polycrystalline aggregates having the same microstructure at a given surface but different 3D grain environments below the surface. Such an ensemble average field indicates the location of most probable plastic slip activity and lattice rotation.
- Fluctuations in the local plastic slip from one realization to another are larger than 60% in 40% of the considered free surface.
- Fluctuations in lattice rotation from one realization to another are larger than 45% in 40% of the considered free surface.
- The choice of a columnar morphology definitely introduces a bias in the estimation of the surface plastic strain field of random polycrystals.

The evaluation of the previous numbers requires, on the one hand, an algorithm to construct random polycrystalline aggregates with a prescribed free surface grain microstructure, and, on the other hand, large-scale 3D finite element simulations. In spite of the high computational effort, there are two limitations in the previous analysis. (i) The number of considered realizations should be higher to improve the estimation of the ensemble average fields and of their variance. (ii) The number of grains at the free surface should be higher to improve the description of the plastic deformation patterns that develop at the free surface. Other limitations deal with the validity of the continuum crystal plasticity framework. The constitutive theory presented in this work is mainly valid for polycrystals with large grains (mm or cm size). More refined models are necessary to account for size effects and dislocation/grain boundary interaction. The continuum modelling of grain size effects was tackled in [28, 29] where additional continuity requirements are enforced at grain boundaries. The modelling of grain boundary behaviour (migration and interaction with dislocation) mainly relies on atomistic simulations and identification of major mechanisms for simplified interface models to be incorporated in continuum crystal plasticity models.

The results presented in this work have severe implications in the way of comparing finite element simulations and strain field measurements that are commonly done in polycrystals. A first requirement is to perform a full 3D finite element analysis of the problem, the 2D approach constraining too much the response of individual grains in random polycrystals. A precise knowledge of the 3D grain morphology is a second prerequisite for a realistic prediction of the strain field in a given set of surface grains. It can be obtained in the case of samples with one grain within the thickness [13], by successive polishing and EBSD mapping of the sample as in [16, 17, 30], or by microdiffraction or neutron diffraction [18, 31, 32]. In many cases, however, this information is not available. A statistical strategy for comparing simulated and measured field quantities is then necessary. Instead of a point-by-point comparison, the simulations and measurements should be carried out on a sufficiently large amount of surface grains. The results can then be analyzed in terms of distribution functions of the observed quantity. Such results are already available from the experimental point of view [26, 31]. The corresponding large-scale 3D finite element analysis remains to be done. This is a necessary step for the ultimate validation of the continuum crystal plasticity theory.

References

[1] J. Mandel, Int. J. Solids Struct. **9** 725 (1973).
[2] R.J. Asaro, Adv. Appl. Mech. **23** 1 (1983).
[3] A.M. Cuitĩno and M. Ortiz, Model. Simul. Mater. Sci. Eng. **1** 225 (1993).
[4] K.K. Mathur and P.R. Dawson, Int. J. Plast. **5** 67 (1989).
[5] S.R. Kalidindi, C.A. Bronkhorst and L. Anand, J. Mech. Phys. Solids **3** 537 (1992).
[6] D.P. Mika and P.R. Dawson, Acta Mater. **47** 1355 (1999).
[7] F. Barbe, S. Forest and G. Cailletaud, Int. J. Plast. **17** 537 (2001).
[8] O. Bouaziz and P. Buessler, Adv. Eng. Mat. **6** 79 (2004).
[9] S.V. Harren and R.J. Asaro, J. Mech. Phys. Solids **37** 191 (1989).
[10] C. Teodosiu, J. Raphanel and L. Tabourot, in *Large Plastic Deformations MECAMAT'91*, edited by C. Teodosiu and F. Sidoroff (Balkema, Rotterdam, 1993), pp. 153–158.
[11] F. Delaire, J.L. Raphanel and C. Rey, Acta Mater. **48** 1075 (2000).
[12] R. Parisot, S. Forest, A.-F. Gourgues, *et al.*, Comput. Mater. Sci. **19** 189 (2001).
[13] F. Eberl, S. Forest, T. Wroblewski, *et al.*, Metall. Mater. Trans. **33A** 2825 (2002).
[14] G. Mohamed, B. Bacroix, T. Ungar, et al., Mater. Sci. Engng. **A234–236** 940 (1997).
[15] A. Bhattacharyya, E. El-danaf, S.R. Kalidindi, *et al.*, Acta Metall. Mater **17** 861 (2001).
[16] J.S. Stölken, in *Material Research Society Fall Meeting, Symposium Z: Multiscale Materials Modeling*, edited by J. Bassani, H. Gao, L. Kubin, *et al.* Selinger (MRS Symposium Proceedings: Boston, 2000).
[17] P. Erieau and C. Rey, Int. J. Plast. **20** 1763 (2004).
[18] S.F. Nielsen, E.M. Lauridsen, D. Juul Jensen, *et al.*, Mater. Sci. Engng A **319–321** 179 (2001).
[19] X. Fu, H.F. Poulsen, S. Schmidt, *et al.*, Scripta Mater. **49** 1093 (2003).
[20] R. Becker and S. Panchanadeeswaran, Acta Metall. Mater. **43** 2701 (1995).
[21] A. Zeghadi, F. N'Guyen, S. Forest, *et al.*, Ensemble averaging stress–strain fields in polycrystalline aggregates with a constrained free surface microstructure – Part 1: computational tools and application to anisotropic elastic behaviour. Phil Mag, this volume (2006).
[22] L. Méric, G. Cailletaud and M. Gasperini, Acta Metall. Mater. **42** 921 (1994).

[23] Z–set package, www.nwnumerics.com, www.mat.Ensmp.fr. (2001).
[24] F. Barbe, S. Forest, S. Quilici, *et al.*, La Revue de Métallurgie **101** 815 (2003).
[25] O. Diard, S. Leclercq, G. Rousselier, *et al.*, Int. J. Plast. **21** 691 (2005).
[26] P. Doumalin, M. Bornert and J. Crépin, Mécanique et Industries **4** 607 (2003).
[27] A.J. Schwartz, M. Kumar and B.L. Adams, *Electron Backscatter Diffraction in Materials Science* (Kluwer Academic, Plenum Publisher, New York, 2000).
[28] S. Forest, F. Barbe and G. Cailletaud, Int. J. Solids Struct. **37** 7105 (2000).
[29] A. Zeghadi, S. Forest, A.-F. Gourgues, *et al.*, Proc. Appl. Math. Mech. **5** 79 (2005).
[30] A. Musienko, Large deformation and damage in crystal plasticity. PhD thesis, Ecole des Mines de Paris, (2005).
[31] N. Letouzé, R. Brenner, O. Castelnau, *et al.*, Scripta Mater. **47** 595 (2002).
[32] D. Gundlach, W. Pantleon, E.M. Lauridsen, *et al.*, Scripta Mater. **50** 477 (2004).
[33] B. Gairola and E. Kröner, Int. J. Engng Sci. **19** 865 (1981).